Takeoff Safety Analysis of High Altitude Long Endurance Aircraft using Integral Quadratic Constraints

Christian Weiser*
German Aerospace Center (DLR), 82234 Weßling, Germany

Felix Biertümpfel†
TU Dresden, 01307 Dresden, Germany
University of Michigan, Ann Arbor, Michigan, 48109, USA

Daniel Ossmann‡
Munich University of Applied Sciences HM, 80335 Munich, Germany

This paper presents a novel methodology to analyze the takeoff phase of High Altitude Long Endurance (HALE) aircraft. Their lightweight structures and the resulting vulnerability to atmospheric disturbances makes operations around the ground, such as takeoff, specifically critical flight conditions. The thereby resulting necessity of a comprehensive verification and validation process is, however, constrained by significant amount of uncertainty in the underlying models due to the complex high-order dynamics originating from the highly flexible structure. This usually results in controller and takeoff safety assessments that require computationally intensive, simulation-based analyses on the full nonlinear aircraft model. To overcome this issue a lean finite-horizon robustness analysis based on the integral quadratic constraint framework is proposed to analyze HALE takeoffs. The study provides analytical upper bounds on the worst-case takeoff performance of the nonlinear model under wind disturbance and model uncertainty. The approach is demonstrated on the German Aerospace Center's HALE platform.

Nomenclature

AoA	Angle of Attack	**IQC**	Integral Quadratic Constraint
AP	Auto-Pilot	**LPV**	Linear Parameter-Varying
BRL	Bounded Real Lemma	**LTI**	Linear Time-Invariant
DLR	German Aerospace Center	**LTV**	Linear Time-Varying
EAS	Equivalent Airspeed	**MC**	Monte-Carlo
FCSW	Flight Control Software	**RDE**	Riccati Differential Equation
HALE	High Altitude Long Endurance	**UAV**	Uncrewed Aerial Vehicle

I. Introduction

High Altitude Long Endurance (HALE) aircraft offer a cost-effective alternative for missions such as surveillance or telecommunications, which are carried out traditionally by satellites in low Earth orbit. Due to their lightweight structures and inherently low control and thrust authority, HALE aircraft are particularly susceptible to wind disturbances. Among the various flight phases, takeoff is especially critical, as the proximity to the ground poses a significant risk of losing both the airframe and the mission [1]. Furthermore, the lightweight design of HALE aircraft leads to highly flexible structural dynamics that are strongly coupled with rigid-body dynamics. This aero-elastic coupling increases the level of uncertainty in flight dynamical models due to the higher model complexity and commonly poorly known structural parameters.

---

[*] Research Associate, Institute of Flight Systems, 82234 Weßling, Germany, AIAA Young Professional

[†] Research Associate, Chair of Flight Mechanics and Control, TU Dresden, 01307 Dresden Germany and Electrical and Computer Engineering, Ann Arbor, Michigan, 48109, USA, AIAA Young Professional

[‡] Professor, Department of Mechanical, Automotive and Aeronautical Engineering, 80335 Munich, Germany, AIAA Senior Member

HALE aircraft are typically launched from specialized carrier structures mounted on trailers towed by vehicles. Following an initial acceleration phase, the aircraft is released and follows an ascent profile, guided by a combination of thrust and pitch commands. The safety of this takeoff procedure is evaluated during the control design and certification process using simulation-based methods applied to the full nonlinear HALE model via Monte-Carlo (MC) simulations or worst-case optimizations. The high level of uncertainty in system dynamics and variability in environmental conditions, however, makes these approaches computationally intensive, as they require a large number of simulations to ensure sufficient coverage. This is undesirable in an iterative control design process. Moreover, simulation-based methods can only yield probabilistic guarantees or lower bounds on worst-case performance metrics. Yet, unidentified worst-case scenarios may lead to catastrophic failures.

Analytical worst-case analyses of suitable linear surrogate models using Integral Quadratic Constraints (IQCs) offer an efficient alternative to simulation-based methods. These approaches provide guaranteed upper bounds on the worst-case performance while being significantly more computationally efficient. The Linear Parameter-Varying (LPV) IQC framework has been successfully applied for robustness analysis of a flexible Uncrewed Aerial Vehicle (UAV) subject to wind disturbances, as demonstrated in [2]. LPV-based methods cover an infinite set of possible parameter trajectories of the system, which makes them broadly applicable. Many aerospace applications, however, only concern a particular trajectory over the predefined time horizon. In such cases, finite-horizon Linear Time-Varying (LTV) IQC methods are more appropriate. These have been successfully used to assess, for example, the touchdown performance of auto-landed aircraft [3] and delivery drones operating in urban environments [4]. The takeoff scenario of a HALE aircraft similarly constitutes a finite-horizon problem, with relatively small variations of the system dynamics along the prescribed ascent trajectory. Therefore, it can be addressed as a special case within the finite-horizon prescribed LTV IQC framework.

Thus, this paper presents the safety analysis of the takeoff phase of the HALE aircraft developed by the German Aerospace Center (DLR) [5] under model uncertainty and wind disturbance, building upon a recent extension of the strict Bounded Real Lemma (BRL) to IQCs, see, e.g., [6] and [7]. Section II details this finite-horizon robustness analysis based on the IQC framework. For the considered HALE aircraft, a baseline controller and an autopilot for the climb phase have already been developed and analyzed in [8, 9]. Section III introduces the dynamics of the aircraft and the associated controller design. The takeoff and the initial seconds of the climb phase, however, have not yet been studied in detail. This segment is particularly well-suited for finite-horizon robustness analysis. The takeoff scenario considered in this work can be divided into the following phases:

1) Takeoff run: The HALE aircraft is mounted on a trailer towed by a ground vehicle and accelerated to the rotation speed V_r.
2) Rotation: The rotation command is issued by the (auto)pilot, pitching the aircraft to the desired climb attitude Θ_{climb}.
3) Initial climb: The aircraft ascends to a safe altitude of at least 5 m above ground, ensuring sufficient ground clearance.

The final altitude of the nominal takeoff scenario is approximately 7 m. Beyond this height, the risk of ground collision or interference with the takeoff vehicle due to, e.g., uncommanded, excessive roll, is significantly reduced. This short time horizon required to reach this altitude makes the scenario particularly suited to finite-horizon analyses. In this study, only the longitudinal dynamics of the aircraft and the corresponding longitudinal controller are considered. Sec. IV presents the application of the proposed robustness analysis to the aforementioned takeoff phase, discusses the results, and finally compares them with data obtained via standard MC simulation techniques.

II. Robustness Analysis over Finite Time Horizons

The takeoff of a HALE aircraft is described by a particular trajectory with a finite time horizon. Thus, it permits the application of a finite-horizon robustness analysis inside the IQC framework. An uncertain finite-horizon linear and possibly time-varying system $F_u(G, \Delta)$ is defined by the feedback interconnection of a nominal LTV system G and an uncertainty Δ. Figure 1 shows such an interconnection. The nominal LTV system G is given by:

$$\begin{aligned} \dot{x}_G(t) &= A_G(t)x_G(t) + B_G(t)\begin{bmatrix} w(t) \\ d(t) \end{bmatrix} \\ \begin{bmatrix} v(t) \\ e(t) \end{bmatrix} &= C_G(t)x_G(t) + B_G(t)\begin{bmatrix} w(t) \\ d(t) \end{bmatrix}. \end{aligned} \tag{1}$$

In Eq. (1), $x_G(t) \in \mathbb{R}^{n_{x_G}}$, $d(t) \in \mathbb{R}^{n_d}$, and $e(t) \in \mathbb{R}^{n_e}$ denote the state, input, and the output vector, respectively. The state space matrices A_G, B_{G_t}, C_{G_t}, and D_{G_t} are continuous and piece-wise bounded functions of time with matching dimensions. The uncertainty $\Delta : L_2^{n_v}[0,T] \to L_2^{n_w}[0,T]$ is a bounded causal operator. The operator Δ can describe nonlinearities, such as actuator saturation, infinite-dimensional operators, e.g., time delays, and dynamic and real parametric uncertainties.

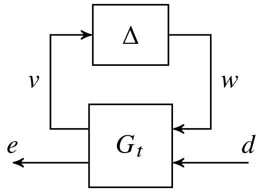

Fig. 1 Interconnection of an LTV system and perturbation.

In this paper, the input-output behavior of a perturbation Δ is bounded via time-domain IQCs. Time-domain IQCs are defined by a filter $\Psi \in \mathbb{RH}_\infty^{n_z \times (n_v+n_w)}$ and a $n_z \times n_z$ real, symmetric matrix M [10]. In case the output z of the filter Ψ fulfills the quadratic time constraint

$$\int_0^T z(t)^T M z(t)\, dt \geq 0 \tag{2}$$

for all $v \in L_2[0,T]$ and $w = \Delta(v)$ over the interval $[0,T]$, the uncertainty Δ satisfies the IQC defined by M and Ψ. If so, the short notation $\Delta \in IQC(\Psi, M)$ is used.

A. Worst-Case Gain Condition

From the worst-case analysis of nominal finite-horizon LTV systems in [11] and the finite-horizon time-domain IQC formulation of the perturbation Δ, a worst-case gain condition can be derived [6, 7]. It provides a guaranteed upper bound on the input-output behavior of uncertain LTV systems over the considered finite analysis horizon.

This facilitates a worst-case analysis condition formulation for the interconnection of a known LTV system G and a perturbation Δ. Given a perturbation satisfying an IQC represented by (Ψ, M), i.e., $\Delta \in IQC(\Psi, M)$, the interconnection $F_u(G, \Delta)$ can be extended by the IQC filter Ψ. This procedure is illustrated in Fig. 2.

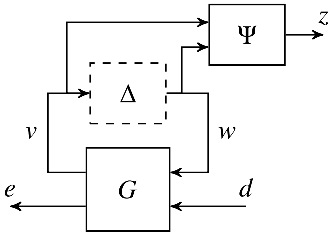

Fig. 2 Feedback interconnection of LTV system G and uncertainty Δ.

The dynamics of this interconnection are represented by

$$\begin{aligned} \dot{x}(t) &= A(t)\,x(t) + \begin{bmatrix} B_1(t) & B_2(t) \end{bmatrix} \begin{bmatrix} w(t) \\ d(t) \end{bmatrix} \\ \begin{bmatrix} z(t) \\ e(t) \end{bmatrix} &= \begin{bmatrix} C_1(t) \\ C_2(t) \end{bmatrix} x(t) + \begin{bmatrix} D_{11}(t) & D_{12}(t) \\ D_{21}(t) & D_{22}(t) \end{bmatrix} \begin{bmatrix} w(t) \\ d(t) \end{bmatrix}, \end{aligned} \tag{3}$$

and denote the extended LTV system H. In Eq. (3), $x(t) \in \mathbb{R}^{n_x}$ represents the state vector containing the states of G and Ψ, $d(t) \in \mathbb{R}^{n_d}$ the disturbance vector, and $e(t) \in \mathbb{R}^{n_e}$ the performance output vector. By enforcing the time-domain inequality Eq. (2) on the filter output z, the explicit representation of the uncertainty $w = \Delta(v)$ is replaced. The finite-horizon worst-case $L_2[0,T]$ to the Euclidean gain is proposed as:

$$\|F_u(G_t, \Delta)\|_2 := \sup_{\Delta \in \mathrm{IQC}(\Psi, M)} \sup_{\substack{d \in L_2[0,T] \\ d \neq 0,\, x(0)=0}} \frac{\|e(T)\|_2}{\|d\|_{2[0,T]}}. \tag{4}$$

The geometric interpretation of this gain is the ball upper bounding the worst-case output $e(T)$ at the final time T over all $\Delta \in IQC(\Psi, M)$ given $\|d\|_{2[0,T]} = 1$, with

$$\|d\|_{2[0,T]} = \left[\int_0^T d^T(t) d(t)\, dt \right]^{\frac{1}{2}}. \tag{5}$$

A dissipation inequality can be stated to upper bound the worst-case $L_2[0,T]$ to Euclidean gain of the interconnection $F_u(G, \Delta)$. It is based on the extended LTV system H given by Eq. (3) and the finite-horizon time-domain IQC formulation in Eq. (2). For a more thorough description, the reader is referred to [6] and [7]. This dissipation inequality is rearranged as an equivalent Riccati Differential Equation (RDE) formulation in the following Theorem 1:

Theorem 1 *Let $F_u(G, \Delta)$ be well-posed $\forall\, \Delta \in IQC(\Psi, M)$, then $\|F_u(G, \Delta)\|_2 < \gamma$ if there exists a continuously differentiable symmetric $P : [0,T] \rightarrow \mathbb{R}^{n_x \times n_x}$ such that*

$$P(T) = \frac{1}{\gamma} C_2(T)^T C_2(T), \tag{6}$$

$$\dot{P} = Q + P\tilde{A} + \tilde{A}^T P - PSP \qquad \forall t \in [0,T], \tag{7}$$

and

$$R = \begin{bmatrix} D_{11}^T M D_{11} & D_{11}^T M D_{12} \\ D_{12}^T M D_{11} & D_{12}^T M D_{12} - \gamma I \end{bmatrix} < 0 \, \forall\, t \in [0,T], \tag{8}$$

with

$$\tilde{A} = \begin{bmatrix} B_1 & B_2 \end{bmatrix} R^{-1} \begin{bmatrix} (C_1^T M D_{11})^T \\ (C_1^T M D_{12})^T \end{bmatrix} - A, \quad S = -\begin{bmatrix} B_1 & B_2 \end{bmatrix} R^{-1} \begin{bmatrix} B_1^T \\ B_2^T \end{bmatrix} \tag{9}$$

and

$$Q = -C_1^T M C_1 + \begin{bmatrix} (C_1^T M D_{11})^T \\ (C_1^T M D_{12})^T \end{bmatrix}^T R^{-1} \begin{bmatrix} (C_1^T M D_{11})^T \\ (C_1^T M D_{12})^T \end{bmatrix}. \tag{10}$$

Proof: The proof is provided in [12]. □

The RDE in Eq. (7) is a stiff ordinary differential equation [13]. Thus, in this paper, it is solved with the Matlab internal solver `ODE15s` [14]. The computational effort scales with the length of the analysis horizon as well as the complexity and size of the IQC parameterization. Especially the latter makes the RDE numerically harder to solve due to adverse effects on its conditioning.

B. Worst-Case Gain Computation

In general, an infinite number of IQCs exist to describe a given uncertainty. The most common approach found in literature, see, e.g., [15] or [16], is to select a fixed filter Ψ and parameterize M. This means the IQC matrix M is confined to a feasibility set $\mathcal{M}$ such that $\Delta \in IQC(\Psi, M)$ for all $M \in \mathcal{M}$. The analysis conducted in this paper covers perturbations in the form of full-block Linear Time-Invariant (LTI) dynamic uncertainties. An example of a feasible parameterization of such an uncertainty type is shown in Example 1.

Example 1 *Let Δ be a full-block LTI dynamic uncertainty, with $\Delta \in \mathbb{RH}_\infty$ and $\|\Delta\|_\infty \leq b \in \mathbb{R}$. A valid time-domain IQC for Δ is defined by $\Psi = \left[\begin{smallmatrix} b\psi_\nu \otimes I_{n_\nu} & 0 \\ 0 & \psi_\nu \otimes I_{n_\nu} \end{smallmatrix}\right]$ and $\mathcal{M} := \{M = \left[\begin{smallmatrix} X \otimes I_{n_\nu} & 0 \\ 0 & -X \otimes I_{n_\nu} \end{smallmatrix}\right] : X = X^T > 0 \in \mathbb{R}^{(\nu+1)\times(\nu+1)}\}$. A typical choice for $\psi_\nu \in \mathbb{RH}_\infty^{(\nu+1)\times 1}$ is:*

$$\psi_\nu = \begin{bmatrix} 1 & \frac{s+\rho}{s-\rho} & \ldots & \frac{(s+\rho)^\nu}{(s-\rho)^\nu} \end{bmatrix}^T, \ \rho < 0, \ \nu \in \mathbb{N}_0. \tag{11}$$

In the example above, the matrix variables X and Y are free parameters, whereas ψ_ν is a fixed basis function with pre-selected ν and ρ. By $\otimes$, the Kronecker product is denoted.

Following the described approach, the RDE in Theorem 1 is now parameterized with $M \in \mathcal{M}$. This leads to the corresponding nonlinear optimization problem to minimize γ [12]:

$$\min_{M \in \mathcal{M}} \gamma$$

such that $\forall t \in [0, T]$

$$\begin{aligned} P(T) &= \frac{1}{\gamma} C_2(T)^T C_2(T) \\ \dot{P} &= Q + P\tilde{A} + \tilde{A}^T P - PSP \\ R &< 0. \end{aligned} \tag{12}$$

In [12], an algorithm to efficiently solve the optimization problem is given. This algorithm is based on two nested loops identifying M such that γ is a minimum. In the inner loop, a bisection for a fixed M over γ is conducted. The corresponding outer loop performs a global optimization over $M \in \mathcal{M}$ applying the Log-L-SHADE [12] meta-heuristic to identify the minimal γ. The algorithm provides a set of parameters that allow it to adjust to a specific analysis. These include the search space of the decision variables, the initial population size, i.e., the number of randomized initial guesses in the search space, and the number of population iterations, i.e., the number of decision set iterations. The latter two, in general, scale with the number of decision variables. For more details on recommended settings and their effects, the reader is referred to [12].

III. Closed-Loop HALE Aircraft Simulator

The DLR HALE project has been launched to conduct satellite-like missions, e.g., surveillance and earth observation with optical and radar payloads at a much lower cost than low Earth orbit satellites [5]. One key advantage is the ability to conduct continuous observation of one location or a change of observation location, which is possible at low cost with the HALE aircraft, in contrast to a satellite. The DLR HALE aircraft is projected to fly solar- and battery-powered [17] at an altitude between 60000 ft and 80000 ft with a payload of 5 kg. The wing span is approximately 27 meters, and the total takeoff weight is projected at 136 kg. The aircraft's expected average mission duration ranges from 60 to 90 days. Limiting factors are the available solar energy in higher geographical latitudes and practical considerations, such as the maximum number of flight hours between scheduled maintenance. However, the available solar energy would theoretically allow an unlimited mission duration in certain latitudes. The current aircraft design is shown in Fig. 3. The design and development of the flight control software for the HALE aircraft has been discussed in various previous works, e.g., [8, 9, 18]. The control system design's principal novelty is the special aircraft configuration type and the consideration of flexible aircraft modes for the primary flight control design.

Fig. 3 HALE aircraft rendering (©DLR).

A. Aircraft Model

For the design of the Flight Control Software (FCSW), a flexible flight dynamics model has been implemented based on the model data in references [19–21]. The model uses standard flight mechanics equations of motion [22] as presented, e.g., in the DLR's VarLoads toolchain [23].

The rigid part of the nonlinear equations of motion is defined as

$$\begin{bmatrix} m_{\mathrm{b}}(\dot{\mathbf{V}}_{\mathrm{b}} + \boldsymbol{\Omega}_{\mathrm{b}} \times \mathbf{V}_{\mathrm{b}} - \mathbf{T}_{\mathrm{bE}}\, \mathbf{g}_{\mathrm{E}}) \\ \mathbf{I}_{\mathrm{b}}\dot{\boldsymbol{\Omega}}_{\mathrm{b}} + \boldsymbol{\Omega}_{\mathrm{b}} \times (\mathbf{I}_{\mathrm{b}}\boldsymbol{\Omega}_{\mathrm{b}}) \end{bmatrix} = \boldsymbol{\Phi}_{\mathrm{bg}}\mathbf{P}_{\mathrm{g}}^{\mathrm{ext}}, \tag{13}$$

with the aircraft mass m, its moment of inertia $\mathbf{I}_{\mathrm{b}}$, and the linear and rotational velocities $\mathbf{V}_{\mathrm{b}}$, $\boldsymbol{\Omega}_{\mathrm{b}}$. The flexible equation of motion is defined as a second-order linear equation of the form

$$\mathbf{M}_{\mathrm{ff}}\ddot{\mathbf{u}}_{\mathrm{f}} + \mathbf{D}_{\mathrm{ff}}\dot{\mathbf{u}}_{\mathrm{f}} + \mathbf{K}_{\mathrm{ff}}\mathbf{u}_{\mathrm{f}} = \boldsymbol{\Phi}_{\mathrm{fg}}\mathbf{P}_{\mathrm{g}}^{\mathrm{ext}}, \tag{14}$$

with the mass matrix $\mathbf{M}_{\mathrm{ff}}$, damping matrix $\mathbf{D}_{\mathrm{ff}}$, and stiffness matrix $\mathbf{K}_{\mathrm{ff}}$. The variable $\mathbf{u}_{\mathrm{f}}$ denotes the modal displacement of the structural nodes of the model. The equations Eqs. (13) and (14) have the external forces and moments $\mathbf{P}_{\mathrm{g}}^{\mathrm{ext}}$ on the right-hand side. These are calculated from the aerodynamic and propulsion loads. This procedure is described in more detail in [23]. Additionally, via the force summation method [24], load recovery can be executed. This enables the analysis of structural loads at various cut-points within the aircraft in post-processing. Additionally, the load monitoring stations can be set as an output during linearization. This possibility can be used later in a Verification framework to determine the influences of the controller on the peak structural loads.

The above-presented nonlinear model serves to generate linear models of the form

$$\left[\begin{array}{c} \dot{x} \\ \hline y \end{array}\right] = \left[\begin{array}{c|cc} A & B_u & B_d \\ \hline C & D_u & D_d \end{array}\right] \left[\begin{array}{c} x \\ \hline u \\ d \end{array}\right], \tag{15}$$

which are used for linear control design using robust control design methods. The vector x denotes the state vector, including relevant rigid body and flexible states, u is the control input, i.e., control surface deflection angles, y denotes the output vector, and d is the disturbance vector added after linearization.

B. Control Laws

The control structure is selected as a cascaded architecture [8] (gray background area in Fig. 4), consisting of an inner loop, which tracks in the longitudinal axis the pitch attitude Θ via the elevator command η. The outer cascade is the Auto-Pilot (AP) that follows commands in the climb rate $\dot{h}$, and Equivalent Airspeed (EAS). For the analysis of the takeoff problem, the longitudinal axis only is depicted; the complete control laws are described in [8, 25]. On the right-hand side, not included in the control software, G_{AC} denotes the nonlinear, flexible aircraft dynamics including sensors and actuators. For the control design, the actuators and sensors are simplified as second-order dynamics and a delay approximation.

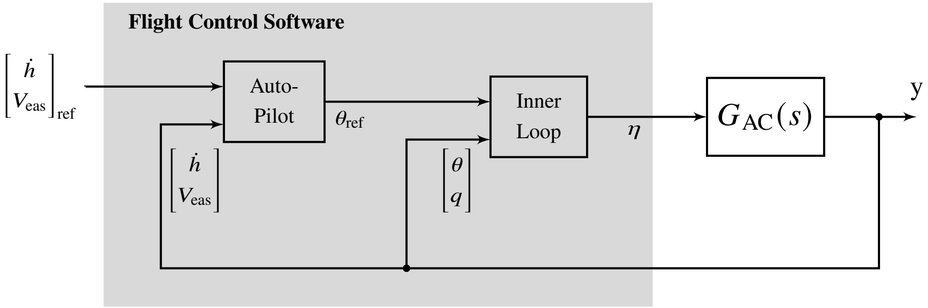

Fig. 4 Longitudinal flight control architecture diagram.

From Fig. 4, the following four main control modes can be derived:

1) Manual Mode: the pilot command is mapped to the control surfaces, and no protection algorithms are active.
2) Augmented Mode: the inner loop rate command / attitude hold control law is active, and the pilot command is interpreted as a pitch rate command.

3) Flight Path Mode: the autopilot controls the flight path vector with the entries airspeed, and climb rate command ($[\dot{h}, V]^T$), defined by the operator. If only airspeed is defined, the thrust can be set manually by the operator, and the corresponding climb rate for the selected airspeed and thrust is acquired as a consequence.
4) Managed Mode: a flight management system, which is not part of the FCSW, controls the aircraft trajectory and provides the flight path vector command.

For the takeoff scenario, the FLIGHT PATH MODE is used with the references EAS and thrust set to climb power.

C. Simulation Framework

Both simulation analysis techniques use a high-fidelity aircraft model of the DLR HALE aircraft. Figure 5 depicts the closed-loop simulation model, which is an interconnection of the described aircraft model with the FCSW. This model has been generated using the nonlinear flexible aircraft dynamics presented in Eqs. (13) and (14). The propulsion system is modeled as a proportional linear system of first-order, and the rotational speed n is converted to thrust via a detailed look-up table providing the thrust coefficient based on the propeller advance ratio $J = \frac{V_a}{nD}$ using the true airspeed V_a and the propeller diameter D. Sensor models are added to estimate the delay and noise of the original system such that an overall realistic high-fidelity aircraft model is achieved.

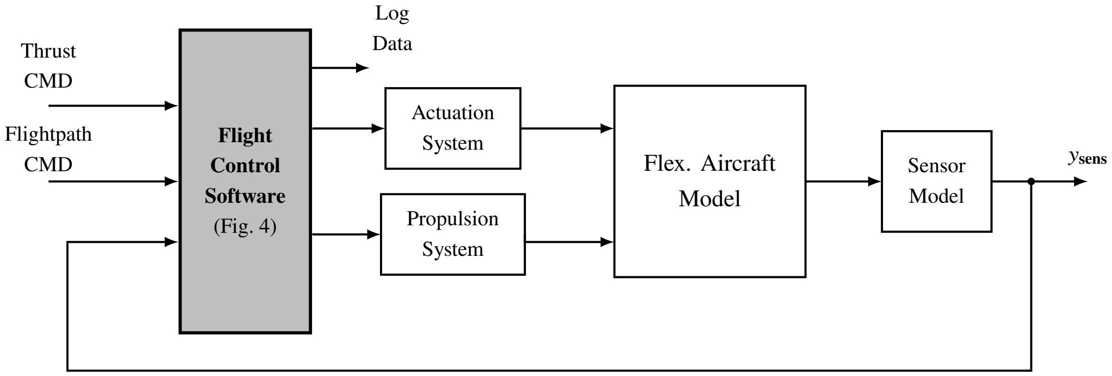

Fig. 5 Schematic illustration of the HALE simulation environment.

D. Atmospheric Disturbance Modeling

The main factor for external disturbances to be considered are atmospheric disturbances. The wind field induced by a discrete gust can be described using the gust gradient H, the gust amplitude U_{ds}, and the gust start time t_s, as detailed in CS / FAR 25.341 [26] via

$$u_g = \begin{cases} \frac{U_{\text{ds}}}{2}\left(1 - \cos\left(\frac{\pi x_j}{H}\right)\right) & , \quad 0 \le x \le 2H \\ 0 & , \quad x > 2H. \end{cases} \tag{16}$$

For modeling continuous turbulence, the Dryden spectrum [27, 28] is used, as suggested in the certification requirements [26]. An analysis of the interaction of the HALE autopilot with worst-case turbulence has already been investigated in [9]. For the takeoff analysis herein, however, the focus needs to be placed on worst-case 1-cosine gusts occurring during the initial takeoff phase, as these have the dominant impact on takeoff performance.

To enable a meaningful comparison between individual simulation runs while allowing variations in the gust parameters, in particular the gust gradient H, the energy of the gust must be kept constant across all cases. The energy of the gust velocity signal defined in Eq. (16) is given by

$$E_g = \int_0^{2H} u_g^2 \, dx = \frac{3}{4} U_{\text{ds}}^2 H, \tag{17}$$

which explicitly depends on the gust gradient. The default parameterization is made for a disturbance signal energy of 1.2 and values for H ranging from 5 m to 35 m. The lower bound of the gust length is taken from [25]. The upper bound follows from the analyzed time horizon of 7 s from the disturbance initiation until the simulation end, and the relation $2H = V_{\text{to}} t$ where V_{to} is the take-off velocity.

IV. Analysis of the HALE Aircraft Takeoff Scenario

For the analysis of the takeoff, the LTI model Eq. (15) of the aircraft's longitudinal dynamics is defined the state vector including the rigid body states, which are airspeed V, pitch attitude Θ, Angle of Attack (AoA) α, pitch rate q, and altitude. Furthermore, flexible modes U_f are considered to account for the correct model dynamics [8]. The overall dynamics are described by the system G_{lon} in the time domain. In that style, the systems G_{act} and G_{prop} represent the actuator and propulsion system modeled as first-order dynamics, respectively. Figure 6 illustrates the closed-loop aircraft system augmented by uncertainties covered by Δ for the worst-case analysis. This uncertainty is introduced in the elevator channel in the form of disk-margin-like input disturbance, as depicted in Fig. 6. The flight controller (K_V, K_Θ) is the cascaded control system introduced in Fig. 4 with a fixed set-point V_{ref} which is the nominal operational speed. The feedback values to the controller are the rigid body states of the aircraft (V, Θ, q). Further, a wind disturbance d_{gs}, e.g., by a gust, is added as an input to the plant. The altitude output h is the analyzed quantity that is assessed. The performance analysis metric is the altitude deviation $\delta_h = |h_{\text{ref}} - h|$ from the nominal reference trajectory h_{ref} without wind disturbance input and $\Delta = 0$. For the takeoff scenario, the aircraft is trimmed at sea level at the takeoff velocity $V_{\text{eas}} = V_{\text{to}}$. At $t = 5$ s, the rotation is initiated, and the throttle input is set to climb power between 4 s and 7 s. Further, at $t = 8$ s, the wind disturbance starts.

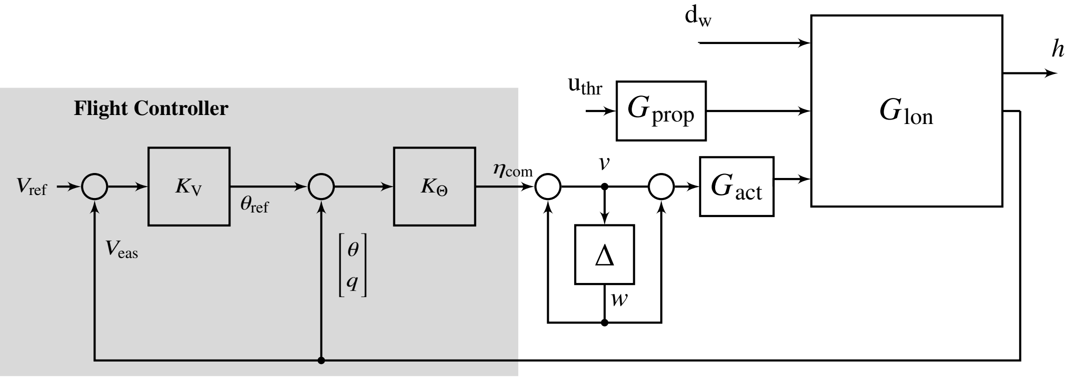

Fig. 6 Worst-case analysis interconnection.

A. Finite Time Horizon Analysis

A typical robustness quantification for control-augmented aircraft is given by gain and phase margins. These quantify the maximum individual gain or phase perturbation a closed-loop can tolerate before becoming unstable. The LTV analysis applies symmetric disk margins (see, e.g., [29]), which permit simultaneous perturbations in gain and phase inside a predetermined disk. This relates the analysis to classical certification processes, i.e., we analyze if the HALE safely takes off under perturbations inside the disk. The HALE's design gain and phase margin are 9 dB and 55 deg, respectively, and cover the expected uncertainties in the system. A disk margin matching these values provides thus a conservative and safe "over-approximation" of classical stability requirements of 6 dB gain and 45 deg phase margins.

A disk margin-like perturbation can be easily integrated into the closed-loop using a dynamic uncertainty Δ, with $\|\Delta\|_\infty \leq b \in \mathbb{R}^+$. Figure 6 depicts the analysis interconnection for a symmetric input disk perturbation allowing an analysis in the LTV IQC framework. The norm bound b of Δ relates to a gain perturbation in the interval $[\frac{1-b}{1+b}, \frac{1+b}{1-b}]$. The simultaneous phase perturbation is confined to the interval $[-2\tan^{-1} b, 2\tan^{-1} b]$. The interconnection in Fig. 6 is transformed into the IQC framework described in Sec. II.A. The dynamic LTI uncertainty Δ is represented by the IQC description from Example 1. For the present analysis, ρ is chosen to -1 and ν to 1. All other settings are left at the default settings described in [12].

The wind input is scaled by a factor of 1.2. This is equivalent to the $L_2[0, T]$ norm of the largest expected, sensible gust in the nonlinear analysis as described in Section III.D. The term sensible refers to the amount of energy the gust may have so that the aircraft propulsion system can cope with the disturbance. Note that the certification gust proposed by certification specifications for passenger aircraft would lead to a loss of aircraft due to the limited amount of control authority and cannot be directly applied to HALEs. The IQC analysis considers a worst-case distribution of signal energy, which by definition covers the gust. Hence, the analysis provides a worst-case of the external wind disturbance.

The analysis is first performed for the aforementioned design margins, which correspond to $b = 0.51$. The resulting worst-case value of the altitude perturbation at the end of the analysis horizon is -4.0 m. Note that the analysis condition only provides an absolute value of the worst-case altitude deviation, but the worst-case direction is obvious. The analysis is completed in approximately 150 s on a desktop computer with 16 cores and 96 GB of memory.

Next, the maximum disk margins for which the HALE can still perform a safe take-off is identified. Therefore, the analysis is repeated for uncertainty norm bounds starting from $b = 0.001$ (effectively no perturbation), which are increased by a step size of 0.1 until the algorithm fails to provide a (feasible) worst-case value. Around the failure region, the analysis step size is reduced to get a precise estimate of the maximum b. Figure 7 depicts the results for the different values of b. The design margin of the system ($b = 0.51$) is marked in red. The maximum b for which a feasible solution was found is $b = 0.53$. For larger disk margins, the system becomes "unstable". However, the first b for which h_{wc} is large enough to cause an impact is 0.54, which corresponds to a gain and phase margin of 10 dB and 57 deg, respectively. The analysis is completed in $\leq$ 30 min on the aforementioned desktop computer.

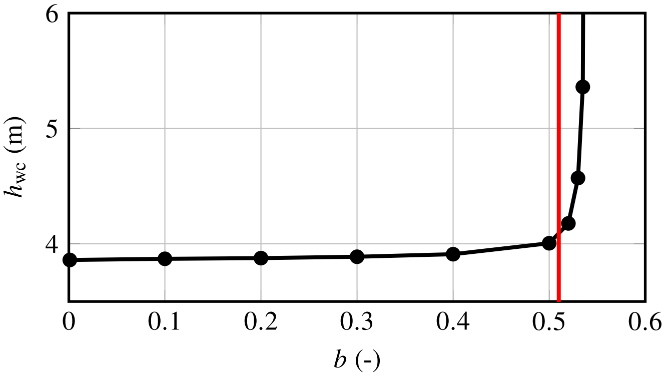

Fig. 7 Worst-case altitude deviation for values of b vs. value of b for the system margins (—).

B. Monte-Carlo Simulation

For an evaluation of worst-case found by the finite-horizon analysis in Sec. IV.A, a MC analysis is conducted. The MC simulation shall prove that we calculated a worst-case by comparing the finite horizon analysis altitude deviation to the altitude signal obtained from non-linear simulations which are disturbed by 1-cosine gusts of different gust length parameters (but with the same energy each).

In a first step, the nominal (zero-wind) takeoff, and the worst-case wind signal obtained by the finite horizon analysis are set as disturbance signals in the nonlinear simulation. Figure 8 shows the altitude trajectory of the nominal, undisturbed nonlinear simulation scenario (—), and the worst-case wind signal found in Sec. IV.A as a disturbance input (—). The time $t = 0$ s denotes the moment when the aircraft takes off from ground. The worst-case wind disturbance signal is calculated from the nominal formulation of Theorem 1 following the explanations in [30]. For the

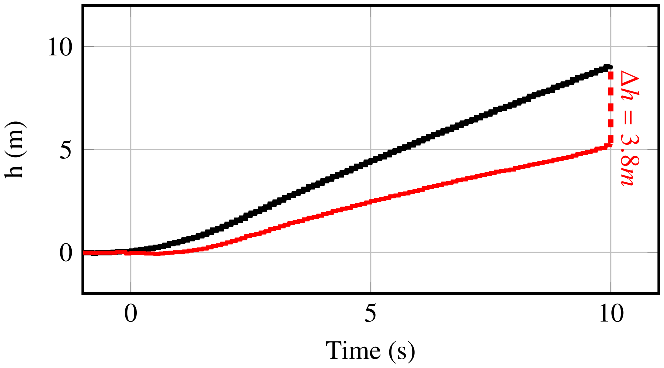

Fig. 8 Comparison between nominal take-off simulation (—) and worst-case wind disturbance (—) from the finite time horizon analysis.

final time of 10 s, the finite horizon worst-case disturbance causes an altitude deviation from the nominal simulation of 3.8 m, which is almost identical to the result for $b = 0.001$ (4.1 m) in Sec. IV.A.

The high-fidelity nonlinear simulator of the aircraft described in Sec. III is parameterized for the MC simulation in the following way: free parameters for the MC analysis are the initial take-off equivalent airspeed, which may vary by ±1 m/s, which is the allowed range for safe operation of the vehicle. For the velocity, a uniform distribution is used. Additionally, the pitch damping coefficient C_{mq} and the pitching moment $C_{m\alpha}$ are varied by ±15% each using a normal distribution. The gust gradient H is varied from 5 to 35 m in a uniform distribution and the gust amplitude is adjusted as described in Sec. III.D to keep the disturbance energy constant. For verification in this work, $n = 1000$ simulations are performed. The computational time for the presented MC simulation is approximately 1 h when using 16 cores (3 GHz each) which is already double the time of the LTV analysis on the same machine for this relatively low number of MC evaluations. The resulting cumulative distribution function (CDF) of the Monte-Carlo analysis is depicted in Fig. 9a, where the difference of the final altitude of the individual parameterized and the nominal simulation is evaluated, $\Delta h_i = h_{\mathrm{MC},i}(t_{\mathrm{end}}) - h_{\mathrm{nom}}(t_{\mathrm{end}})$. The red area in Fig. 9a illustrates the upper bound for the altitude deviation δH found by the LTV analysis. As expected, the results of the MC simulation lie below this bound which backs the assumption that indeed the worst-case flight path deviation for the assumed worst-case disturbance is found.

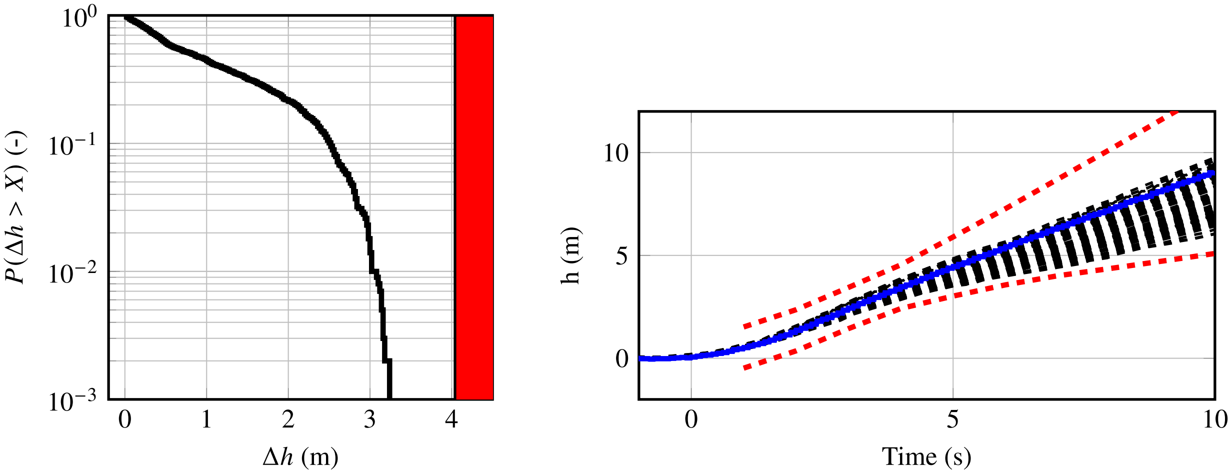

(a) Cumulative distribution function.

(b) Nominal (—) and disturbed (- - -) altitude signals from the nonlinear Monte-Carlo simulation versus worst case bounds (- - -).

Fig. 9 Verification results showing the CDF of the altitude deviation at the end of the simulation from the Monte-Carlo simulation in (a), and the determined worst case bounds over the time horizon in (b).

For additional verification, the finite time horizon analysis is performed with finite time horizon values of $T = 1, 2, \ldots, 10\,s$, $b = 0.5$ and a constant wind scaling of 1.2. The corresponding worst-case values are used to form the worst-case bounds depicted in Fig. 9b. Note that this is necessary, as Theorem 1 only provides an upper bound at the final time T. It is shown, that all altitude responses of the nonlinear MC simulations are also within the worst-case envelope. This confirms the effectiveness of the approach to provide upper bounds for the nonlinear simulation and indicates that the proposed finite horizon IQC analysis provides a valuable complement to expensive Monte-Carlo simulations for take-off analyses of HALE aircraft at a much lower computation cost.

V. Conclusion

This paper proposes an IQC-based finite time horizon robustness analysis for the takeoff scenario of a HALE aircraft. By formulating the plant-uncertainty interconnection as an extended LTV system interconnected with a disk-margin based uncertainty, the analysis predicts an upper bound for the performance output under the influence of disturbances. This upper bound is validated by non-linear simulations and Monte-Carlo analysis. The results suggest that IQC-based finite-horizon analysis offers a practical tool for rapid robustness checks providing an upper bound for performance signals under input disturbances with bounded signal energy.

References

[1] Anderson, J. D., *Aircraft performance and design*, WCB/McGraw-Hill, Boston, Mass., 1999.

[2] Knoblach, A., Pfifer, H., and Seiler, P. J., "Worst Case Analysis of a Saturated Gust Loads Alleviation System," *AIAA Guidance, Navigation, and Control Conference*, Kissimmee, FL, USA, 2015.

[3] Biertümpfel, F., and Pfifer, H., "Finite horizon analysis of autolanded aircraft in final approach under crosswind," *Control Engineering Practice*, Vol. 122, 2022, p. 105105.

[4] Thiele, F., Biertümpfel, F., and Pfifer, H., "Finite-Horizon Robustness Analysis under Mixed Disturbances using Signal-IQCs," *11th IFAC Symposium on Robust Control Design*, Porto, Portugal, 2025.

[5] Nikodem, F., "Overview of the DLR High Altitude Platform and Scientific Potential of the Technology Demonstrator HAP-Alpha," *Deutscher Luft- und Raumfahrtkongress*, Stuttgart, Germany, 2023.

[6] Biertümpfel, F., and Pfifer, H., "Worst Case Gain Computation of Linear Time-Varying Systems over a Finite Horizon," *IEEE Conference on Control Technology and Applications*, Copenhagen, Denmark, 2018, pp. 952–957.

[7] Seiler, P., Moore, R. M., Meissen, C., Arcak, M., and Packard, A., "Finite horizon robustness analysis of LTV systems using integral quadratic constraints," *Automatica*, Vol. 100, 2019, pp. 135–143.

[8] Weiser, C., and Ossmann, D., "Baseline Flight Control System for High Altitude Long Endurance Aircraft," *AIAA SciTech Forum*, San Diego, CA, USA, 2022.

[9] Weiser, C., Ossmann, D., and Pfifer, H., "Robust Path-Following Control for High-Altitude Long-Endurance Aircraft," *AIAA Journal of Guidance, Control, and Dynamics*, Vol. 46, No. 7, 2023, pp. 1416–1424.

[10] Seiler, P., "Stability Analysis With Dissipation Inequalities and Integral Quadratic Constraints," *IEEE Transactions on Automatic Control*, Vol. 60, No. 6, 2015, pp. 1704–1709.

[11] Green, M., and Limebeer, D. J. N., *Linear Robust Control*, Prentice-Hall, Inc., Upper Saddle River, NJ, USA, 1995.

[12] Biertümpfel, F., Pholdee, N., Bennani, S., and Pfifer, H., "Finite Horizon Worst Case Analysis of Linear Time-Varying Systems Applied to Launch Vehicle," *IEEE Transactions on Control Systems Technology*, Vol. 31, No. 6, 2023, pp. 2393–2404.

[13] Abou-Kandil, H., Freiling, G., Ionescu, V., and Jank, G., *Matrix Riccati Equations in Control and Systems Theory*, Birkhäuser, Basel, 2003.

[14] MATLAB, *R2020b*, The MathWorks Inc., Natick, Massachusetts, 2020.

[15] Pfifer, H., and Seiler, P., "Robustness analysis of linear parameter varying systems using integral quadratic constraints," *International Journal of Robust and Nonlinear Control*, Vol. 25, No. 15, 2014, pp. 2843–2864.

[16] Veenman, J., Scherer, C. W., and Köroğlu, H., "Robust stability and performance analysis based on integral quadratic constraints," *European Journal of Control*, Vol. 31, 2016, pp. 1–32.

[17] Mayer, S., Bierig, A., and Ossmann, D., "Thermal Modeling of the Power Train of Solar Powered High Altitude Aircraft," *Deutscher Luft- und Raumfahrtkongress*, 2024.

[18] Weiser, C., Schulz, S., Voß, A., and Ossmann, D., "Attitude Control for HALE Aircraft Considering Structural Load Limits," *AIAA SciTech Forum*, National Harbor, MD, USA, 2023.

[19] Hepperle, M., "Aerodynamic Design and Analysis - HAP-Omega-6," Tech. rep., Institute of Aerodynamics and Flow Technology, German Aerospace Center (DLR), 2022.

[20] Voß, A., Koch, C., Niemann, S., Handojo, V., and Weiser, C., "Transition From Preliminary to Detailed Design of a Highly Elastic Solar Electric Aircraft," *International Forum on Aeroelasticity and Structural Dynamics*, Madrid, Spain, 2022.

[21] Hasan, Y. J., Roeser, M. S., Hepperle, M., Niemann, S., Voß, A., Handojo, V., and Weiser, C., "Flight mechanical analysis of a solar-powered high-altitude platform," *CEAS Aeronautical Journal*, Vol. 14, No. 1, 2022, pp. 201–223.

[22] Waszak, M. R., and Schmidt, D. K., "Flight dynamics of aeroelastic vehicles," *AIAA Journal of Aircraft*, Vol. 25, No. 6, 1988, pp. 563–571.

[23] Kier, T. M., Looye, G., and Hofstee, J., "Development of Aircraft Flight Loads Analysis Models with Uncertainties for Pre-design Studies," *International Forum on Aeroelasticity and Structural Dynamics*, Munich, Germany, 2005.

[24] Bisplinghoff, R. L., Ashley, H., and Halfman, R. L., *Aeroelasticity*, Dover Publications, Incorporated, 2013.

[25] Weiser, C., "Verification and Clearance of a Flight Control System for High Altitude Long Endurance Aircraft," *IEEE Aerospace Conference*, Big Sky, MT, USA, 2025.

[26] European Aviation Safety Agency, "Certification Specifications and Acceptable Means of Compliance for Large Aeroplanes CS-25," , 2023.

[27] U.S. Department of Defense, "MIL-HDBK-1797: Flying Qualities of Piloted Aircraft," , 2004.

[28] Hoblit, F. M., *Gust Loads on Aircraft: Concepts and Applications*, American Institute of Aeronautics and Astronautics, 1988.

[29] Seiler, P., Packard, A., and Gahinet, P., "An Introduction to Disk Margins," *IEEE Control Systems*, Vol. 40, No. 5, 2020, pp. 78–95.

[30] Iannelli, A., Seiler, P., and Marcos, A., "Worst-Case Disturbances for Time-Varying Systems with Application to Flexible Aircraft," *Journal of Guidance, Control, and Dynamics*, Vol. 42, No. 6, 2019, pp. 1261–1271.